Elastography: A Systems Approach

Jonathan Ophir,[1] Faouzi Kallel,[1,2] Tomy Varghese,[1] Michel Bertrand,[2] Ignacio Céspedes,[1] Hari Ponnekanti[1]

[1]University of Texas Medical School, Department of Radiology, Ultrasonics Laboratory, 6431 Fannin St., Houston, TX 77030
[2]Institute of Biomedical Engineering, Ecole Polytechnique, C.P./PO Box 6079, succ. Centre-Ville, Montreal, Quebec, Canada

Received 11 June 1996; revised 3 October 1996

ABSTRACT: We present a review of elastography from a systems point of view. We show that elastography can be viewed as a cascade of two distinct processes. The first process involves the mapping of the distribution of local elastic moduli in the target into a distribution of local longitudinal strains. This process is governed by the theory of elasticity as applied to a particular experimental setup under some specific boundary conditions and some assumptions. Since this process involves errors due to the simplified mechanical model used, artifacts such as target hardening, stress concentrations, and limited contrast-transfer efficiency are usually encountered. These errors may be recursively minimized by solving the inverse problem, thus increasing the contrast-transfer efficiency such that a more accurate modulus image may be obtained. The second process involves the production of the strain image (elastogram) from ultrasonically estimated values of local strains. Here, the limitations of the ultrasound system [such as time-bandwidth product, center frequency, and sonographic signal-to-noise ratio (SNR)] as well as the signal-processing algorithms used to process the signals cause additional corruption of the data through the introduction of constraints in the attainable elastographic SNR, resolution, sensitivity, and strain dynamic range. This process is described in terms of a stochastic strain filter. These two system components are discussed in detail, and it is concluded that both must be optimized in a specific order to result in quality elastograms.
 Int J Imaging Syst Technol, **8,** 89–103, 1997

Key words: elastography; elasticity; imaging; ultrasound; strain-filter; inverse-problem

I. INTRODUCTION

The elasticity of soft tissues depends to a large extent on their molecular building blocks (fat, collagen, etc.), and on the microscopic and macroscopic structural organization of these blocks [1]. In the normal breast, for example, the glandular structure may be firmer than the surrounding fibrous connective tissue, which in turn is firmer than the subcutaneous adipose tissue. The standard medical practice of soft-tissue palpation is based on qualitative assessment of the low-frequency stiffness of tissue.

Pathologic changes are generally correlated with changes in tissue stiffness as well. Many cancers, such as scirrhous carcinoma of the breast, appear as extremely hard nodules [2]. In many cases, despite the difference in stiffness, the small size of a pathologic lesion and/or its location deep in the body preclude its detection and evaluation by palpation. In general, the lesion may or may not possess echogenic properties which would make it ultrasonically detectable. For example, tumors of the prostate or the breast could be invisible or barely visible in standard ultrasound examinations, yet be much harder than the embedding tissue. Diffuse diseases such as cirrhosis of the liver are known to increase the stiffness of the liver tissue significantly as a whole [2], yet they may appear normal in conventional ultrasound examination. Since the echogenicity and the stiffness of tissue are generally uncorrelated, it is expected that imaging tissue stiffness will provide new information that is related to tissue structure and/or pathology.

Biologic tissues can be considered as approximating homogeneous gels [3]. Different modes of propagation of elastic waves in such media are determined primarily by their bulk (K) and shear (G) elastic moduli. In biologic soft tissues, $K \gg G$. The bulk properties (and hence, the ultrasonic properties) are determined primarily by the molecular composition of the tissue, while shear properties are determined by the higher level of tissue organization [3]. Since deformable soft tissues are essentially volume-incompressible (i.e., their Poisson's ratio $\nu \sim 0.5$), their shear moduli are proportional to their longitudinal (Young's) moduli [4]. It follows that estimation and imaging of the Young's moduli of tissue should in principle convey information about their shear properties, and hence the higher level of tissue organization.

Strictly speaking, tissue is inelastic [1]. It does not meet the definition of an elastic material, which requires that there be a single valued relationship between stress and strain. Tissue exhibits viscoelastic properties such as hysteresis, stress relaxation, and creep [1]. In addition, it is anisotropic and the strain–stress relationship is nonlinear. When all these factors are coupled, it becomes evident that the problem of how to describe the mechanical properties of tissue requires a significant degree of simplifica-

Correspondence to: J. Ophir
Contract grant sponsor: National Institutes of Health; *Contract grant number:* ROI-CA38515; *Contract grant number:* ROI-CA60520; *Contract grant number:* POI-CA64597
Contract grant sponsor: Diasonics Corporation
Contract grant sponsor: State of Texas

 CCC 0899–9457/97/010089-15

tion. Tissue models that include series (Maxwell model) and parallel (Voigt model) elastic and viscous component have been described [1]. To first approximation, tissue has been assumed isotropic [3,5,6], although there is evidence of anisotropic properties of ultrasound propagation in some soft tissues such as muscle [7]. Even for relatively small strains (<10%), tissue exhibits nonlinear behavior and hysteresis [6]. Thus, the elastic properties of tissue may be better defined if they are specified at a given operating strain or stress [5–7].

Quantitative measurements of the elastic properties of tissue reported in the past resulted in a wide range of values [1,6]. The vast majority of the research on the mechanical properties of tissues has been done for tissues that are subject, actively or passively, to some degree of mechanical activity (muscles, arteries, lung, tendons, bone, skin, and ureter). In contrast, very little quantitative information is available on the elastic properties of the tissue in organs that do not have mechanical activity (breast, prostate, thyroid, testes, etc.). A limited set of *in vitro* measurements of the elastic moduli of prostate and liver tissues was described by Parker et al. [6]. In a presentation by Sarvazyan [8] the results of a study involving 162 *in vitro* samples of normal, cancerous, and fibroadenomatous breast tissues were described. The average shear moduli indicate that normal breast tissue is approximately four times softer than fibroadenoma tissue [8]. Breast cancer showed a wide range of shear moduli which can be up to seven times higher than those of normal tissue [8]. Walz et al. [9] presented results of an *in vivo* study involving 250 breast lesions which indicate that fibroadenomas are approximately eight times softer than carcinomas.

Qualitative description of the hardness of pathologic tissues can be found in the medical literature. Malignant lesions are generally present as hard nodules, e.g., scirrhous carcinoma of the breast, liver metastases, prostatic carcinoma, and thyroid cancer [2]. While scirrhous carcinoma of the breast, which is the most common cancer of the breast and constitutes about three fourths of all breast cancers, is known to be very hard, other types of breast cancers (e.g., intraductal and papillary carcinoma) are soft [10]. Benign fibrocystic disease has been known to be extremely hard on very rare occasions and the glandular tissues of the breast are firm in relation to the soft fatty areas [11].

Substantial work has been done concerning the mechanical properties of skin as summarized by Mridha and Ödman [12,13]. Edematous tissue incurs an increase in stiffness with a substantial increase in the fluid flow in the subcutaneous tissue. A mechanical model of tissue [14] considers the tissue as composed of an elastic component (fibers) and two viscous components (gellike material and fluid). Based on this model, a noninvasive technique has been developed to measure the resistive force of tissue under compression [13].

Truong et al. [15] applied mechanical waves with frequencies ranging from 100 Hz to 10 kHz to the ends of whole frog sartorius muscles. By measuring the speed of propagation and wave attenuation the effects of muscle contraction on the elastic properties of skeletal muscle were investigated. Levinson [7] measured the four elastic constants of frog sartorius muscles associated with a transversely isotropic model of muscle tissue. Krouskop et al. [5] measured ultrasonically the Young's modulus of human muscle *in vivo* under relaxed, mild, and maximum contraction, showing several fold changes among contraction states. Parker et al. [6] reported order-of-magnitude differences among stiffnesses of different tissue specimens such as muscle and prostate, ranging approximately from 1 kPa to 1 MPa.

The limited information about the elastic properties of tissue and the changes of these properties due to disease presents a fundamental challenge in the development of elastography, since we attempt to image a tissue parameter without quantitative knowledge of its true magnitude and changes due to disease. Moreover, methods for such quantitative measurements are not yet well developed.

In the last 15 years there has been a slow but steady stream of papers describing various methods to estimate and image the elasticity of soft tissues. These include Doppler techniques and time-domain techniques. The reader is referred to a recent review article that summarizes these techniques and includes a large number of the pertinent references [16]. In this article we concentrate on a particular technique we call elastography, which we have been developing in our laboratory in the past 5 years [17]. This technique involves the application of a quasi-static compression to the tissue, and the production of an image (elastogram) that depicts the distribution of the estimated strains in the tissue. We take a systems approach to the description of elastography, where we view the process of generating an elastogram as a two-step process (Fig. 1):

1. The mapping of the elastic modulus distribution in tissue into a distribution of strains. This process is governed by the basic physics as expressed in the elasticity equations (including some assumptions about their applicability), which are dependent on the modulus distribution itself, the details of the applied compression, and the boundary conditions. If we make the simple (but generally inaccurate) assumption of stress constancy and a semi-infinite target, there is an inverse proportionality between the modulus distribution and the strain distribution. This assumption generally results in significant mechanical artifacts in the elastogram. A preferred method is to use inverse problem (IP) methods [31–35] combined with additional information to reduce the level of the mechanical artifacts.
2. The mapping of the distribution of strains into an elastogram. This step consists of the application of ultrasonic techniques to the estimation of the strain distribution. The technical parameters [center frequency, bandwidth, gate length, and sonographic signal-to-noise ratio (SNR)] as well as the particulars of the signal processing algorithm are combined in a so-called strain filter to influence the quality of the elastogram in terms of resolution, SNR, sensitivity and dynamic range. A suboptimal strain filter causes image artifacts as well.

Figure 2 shows these two steps. Figure 2(a) shows a simulated elasticity modulus distribution; Figure 2(b) shows the concomitant strain distribution, and Figure 2(c) shows the mapping of the strain into an elastogram.

II. ELASTOGRAPHY: A SYSTEMS APPROACH

A. The Elastography Technique. We recently introduced a new method termed elastography for direct imaging of the strain and the Young's modulus of tissues [17–20]. Elastography is based on the following principles:

1. The stress applied to the tissue is quasi-static. This essen-

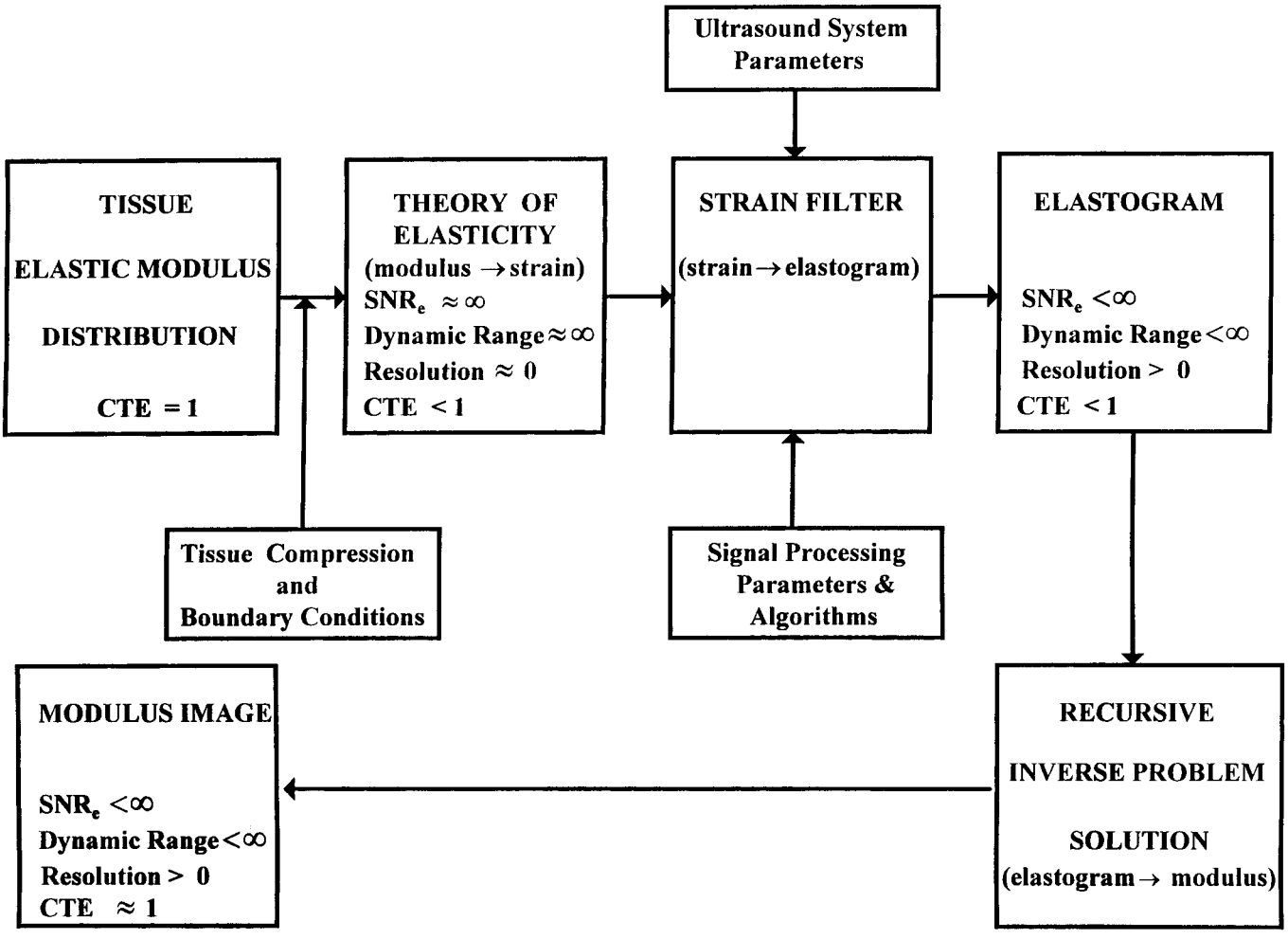

Figure 1. A block diagram of the elastography system. The input to the system is the tissue modulus distribution. The outputs can be either the elastogram (strain image) or the modulus image. The tissue strain obtained by a quasi-static tissue compression, restricted by the mechanical boundary conditions, is measured using the ultrasound system. The block describing the strain filter indicates the filtering of the tissue strains due to the ultrasound system and signal-processing parameters. The strain filter predicts the dynamic range and respective SNR_e at a given resolution in the elastogram. The contributions of the signal-processing and ultrasound system parameters and other algorithms are indicated as inputs into the strain filter. The optimized elastogram is used as an input to the recursive inverse problem solution block where the CTE [see Equation (9)] is improved with subsequent reduction of artifacts in the final modulus image.

tially avoids problems due to reflections, standing waves, and mode patterns that may interfere with quality image formation;

2. The applied quasi-static uniaxial stress reduces the complexity of the generalized viscoelastic equation of forced motion of the form

$$M\frac{d^2x}{dt^2} + R\frac{dx}{dt} + Kx = F_0e^{j\omega t}$$

that contains inertial (M), viscous (R), and stiffness (K) controlled terms, where x is the displacement, F_0 is the force amplitude, and ω is the angular vibrational frequency). The reduced form is the much simpler Hookean equation $Kx = F_0$; since $\omega = 0$ and x is a constant, the velocity and acceleration terms vanish. In principle, this allows the isolation and direct extraction of the local tissue stiffness parameter (K) from measurement of the differential applied force (or stress) F_0 and the resulting local changes in displacement x. Determination of the global stiffness of gels and of human muscle *in vivo* using static force was reported by Mridha and Ödman [12,13].

3. The average levels of strain evoked in the tissue are very small (on the order of 0.01 or less). These strain levels are considered small enough to keep the Hookean equation well within the linear range, based on the linear stress/strain relationships for gels and human muscle *in vivo* reported by Mridha and Ödman [12] which were valid up to a strain level of 0.25. They are also kept small to keep the distortion in the time-shifted echo signals to a minimum, hence maintaining a low level of decorrelation noise in the elastogram (more on this later); and
4. Elastography is capable of producing high-resolution images [20].

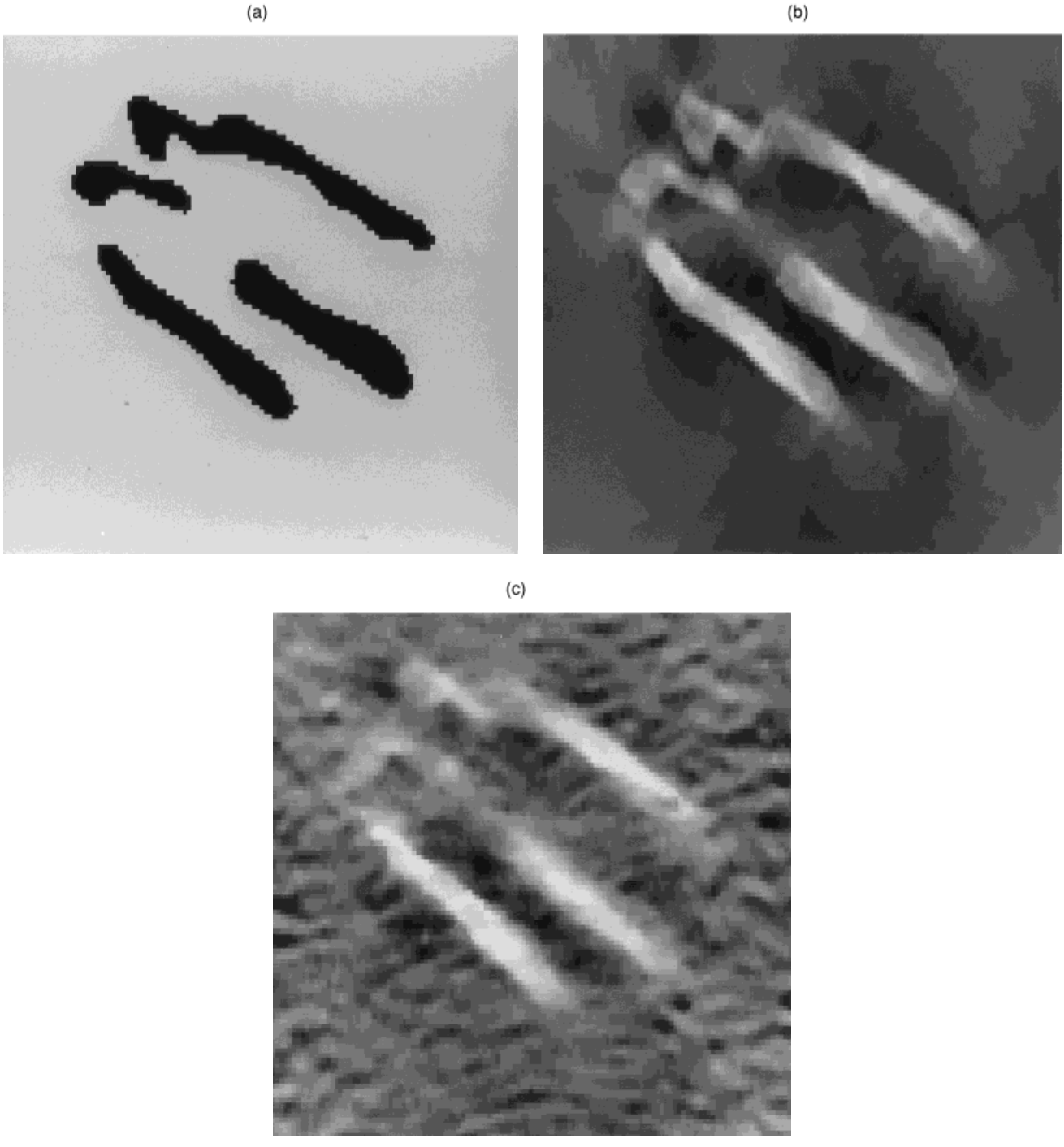

Figure 2. The elastography process from a modulus distribution to an elastogram (simulation). (a) An modulus distribution consisting of a homogeneous embedding elastic inhomogeneities of arbitrary shape. These modulus inhomogeneities are 10 times softer than the background and thus may represent uniform fat tissue embedded in a piece of beef muscle tissue. (b) Strain image of the elasticity distribution shown in (a) resulting from the application of a uniform 1% axial compression and assuming a slip boundary condition on both the top and the bottom. Observe artifactual strain disturbances inside and outside the fatty areas due to the assumption of stress uniformity. (c) Elastogram as computed using correlation techniques applied to pre- and postcompression simulated RF data. Note that (b) and (c) are inverted relative to (a) because of the general inverse relationship between modulus and strain.

When an elastic medium such as tissue is compressed by a constant uniaxial stress, all points in the medium experience a resulting level of longitudinal strain whose principal components are along the axis of compression. If one or more of the tissue elements has a different stiffness parameter from the others, the level of strain in that element will be higher or lower; a harder tissue element will generally experience less strain than a softer one. The longitudinal strain is estimated in one dimension from

the analysis of ultrasonic signals obtained from standard medical ultrasound diagnostic equipment. This is accomplished by acquiring a set of digitized radiofrequency echo lines from the tissue region of interest; compressing the tissue with the ultrasonic transducer (or with a transducer/compressor combination) along the ultrasonic radiation axis by a small amount (about $\leq$1%); and acquiring a second, postcompression set of echo lines from the same region of interest. Congruent echo lines are then subdivided into small temporal windows which are compared pairwise using cross-correlation techniques [21], from which the change in arrival time of the echoes before and after compression can be estimated. Because of the small magnitude of the applied compression, there are only small distortions of the echo lines, and the changes in arrival times are also small. The local longitudinal strain may estimated as [17]:

$$e_{11,local} = \frac{(t_{1b} - t_{1a}) - (t_{2b} - t_{2a})}{t_{1b} - t_{1a}} \tag{1}$$

where t_{1a} is the arrival time of the precompression echo from the proximal window, t_{1b} is the arrival time of the precompression echo from the distal window, t_{2a} is the arrival time of the postcompression echo from the proximal window, and t_{2b} is the arrival time of the postcompression echo from the distal window. The windows are translated in small overlapping steps along the temporal axis of the echo line, and the calculation is repeated for all depths. The two fundamental assumptions made are that (1) one-dimensional strain estimation is adequate for meaningful elastograms; and (2) speckle motion adequately represents the underlying tissue motion for small uniaxial compression.

The time delays in Equation (1) may be derived by estimating the location of the peak of the crosscorrelation function of the precompression and postcompression echo signals [17]. In the absence of signal decorrelation and under high SNR conditions, a lower bound on the precision of the time-delay estimate may be given by the Cramér-Rao lower bound (CRLB) [22]. For bandpass signals with typical ultrasound center frequencies, bandwidths, observation window lengths, and high SNR, the CRLB for time delays is in the subnanosecond region, which corresponds to the submicron spatial region. For signals with rectangular spectra, the CRLB under these conditions may be evaluated as [e.g., 19,23]:

$$\sigma^2_{CRLB} \cong \frac{1}{4\pi^2 f_0^2 BT \cdot SNR}, \tag{2}$$

where σ^2_{CRLB} = the CRLB on the variance of the estimate; f_0 = the center frequency of the signal; BT = time-bandwidth product; and SNR = sonographic SNR. This expression for the CRLB will be used in a later section to compute some of the limitations imposed by the parameters of the sonographic systems on the attainable quality of the elastogram.

B. Modulus-to-Strain-to-Modulus Transformation. The property of tissue which is of intrinsic interest is the modulus of elasticity. Unfortunately, this quantity is not directly measurable. The only quantity that can be accurately estimated with ultrasound is the local longitudinal strain. There are two basic approaches to deal with this problem:

1. Estimate the local longitudinal strains and display them as an elastogram, assuming a constant or a known distribution of stress; or
2. Obtain additional information such as the distribution of applied force and the boundary conditions, and reconstruct the distribution of the modulus under certain assumptions, using inverse-problem (IP) techniques [31–35].

These approaches are discussed in detail in the following sections.

1. The Assumption of Constant or Known Stress. Linear elastic materials obey the generalized Hooke's law, which states that stress is proportional to strain. The general form of the law is expressed by the statement that each of the components of the state of stress (σ) at a point is a linear function of the components of the state of strain (e) at that point. Mathematically, this is expressed as [4]

$$\sigma_{kl} = C_{klmn} e_{mn}, \tag{3}$$

where the C_{klmn} are elastic constants comprising the elements of a stiffness matrix C. In general, there are 81 such constants corresponding to the indices k, l, m, n taking on values equal to 1, 2, and 3. The symbol σ_{kl} is read as the stress component in a plane perpendicular to the axis indicated by the index k and along the axis indicated by the index l. A similar notation has been used to describe the strain, where m and n have been used to show that a stress component in any direction can be related to the strain component in any other direction through an appropriate elastic constant, which is the reason for the four subscripts for C_{klmn}. By assuming that the material is homogeneous and isotropic, the number of independent constants required to completely characterize the elastic properties of the material reduces to two [4]. These constants are the Lame's constants, λ and μ. The stress–strain relationship for an isotropic, homogeneous material can now be written in the index notation as [4]:

$$\sigma_{kl} = 2\mu e_{kl} + \lambda \delta_{kl} e_{mm}, \tag{4}$$

where δ_{kl} is Kronecker's delta, which is unity when $k = 1$, and zero otherwise. Rearranging and rewriting only the normal (nonshear) terms of Equation (4) in the extended form in terms of local stress, local strain, the Poisson's ratio (ν) and the local Young's modulus (E), we have a set of equations that describe the local Young's moduli E in the target, viz. [4],

$$e_{11} = \frac{1}{E}[\sigma_{11} - \upsilon\sigma_{22} - \upsilon\sigma_{33}] \tag{5a}$$

$$e_{22} = \frac{1}{E}[\sigma_{22} - \upsilon\sigma_{11} - \upsilon\sigma_{33}] \tag{5b}$$

$$e_{33} = \frac{1}{E}[\sigma_{33} - \upsilon\sigma_{11} - \upsilon\sigma_{22}] \tag{5c}$$

where the duplicated subscripts indicate normal components in the corresponding directions, and where

$$\upsilon = \left[\frac{\lambda}{2(\lambda + \mu)}\right] \tag{6a}$$

and

$$E = \frac{\mu[3\lambda + 2\mu]}{\lambda + \mu} \tag{6b}$$

From Equation set (5) it can be seen that to compute the Young's modulus of any element inside a target, at least five of the seven variables must be known. Since most tissues can be treated as incompressible [5], a value close to 0.5 can be assumed for the Poisson's ratio thus reducing the number of variables which must be known to four.

Since the stress components σ_{ii} cannot be measured directly, they must therefore be estimated. The general problem of estimating the various components of stress and strain in a semi-infinite, homogeneous, elastic target that is subjected to a deformation using an externally applied load is known as the Boussinesq problem (after J. Boussinesq [24]). A special case of the problem is the deformation of the target using a rectangular compressor. This problem was investigated in detail by Love [25], who developed mathematical expressions to describe the spatial distribution of the various components of stress as a function of the compressor dimensions and the material properties in homogeneous, isotropic, semi-infinite targets. His expressions for the normal components of stress may be written in their functional form as

$$\sigma_{11} = \sigma_{11}(\sigma_L, x_1, x_2, x_3, a, b) \tag{7a}$$

$$\sigma_{22} = \sigma_{22}(\sigma_L, x_1, x_2, x_3, a, b, \upsilon) \tag{7b}$$

$$\sigma_{33} = \sigma_{33}(\sigma_L, x_1, x_2, x_3, a, b, \upsilon) \tag{7c}$$

where σ_L is the load applied by the compressor; x_1, x_2 and x_3 are the coordinates of the location of interest in the target; and a and b are the length and width of the rectangular compressor, respectively. The expressions in their explicit form are cumbersome and were described completely by Love [25].

In the more practical case where the dimensions of a linearly elastic target are finite along the compression x_1 axis, the principle of superposition could be used to modify Love's theory, as described in Ponnekanti et al. [26]. As a first step in using the principle of superposition, the target can be assumed to be under the influence of two compressors, the compressor on the top that is used to provide the deformation (compressor 1), and the base on which the target is placed (compressor 2). The stress components at any location in the target equal the sum of the corresponding individual components due to the two compressors as if they were acting independently on a semi-infinite medium. Superposition is achieved by simple summation of the corresponding compressive stress components, viz.,

$$\sigma_{11} = \sigma_{11}(\sigma_L, x_1, x_2, x_3, a_1, b_1) + \frac{A_1}{A_2}\sigma_{11}(\sigma_L, d - x_1, x_2, x_3, a_2, b_2) \tag{8a}$$

$$\sigma_{22} = \sigma_{22}(\sigma_L, x_1, x_2, x_3, a_1, b_1, \upsilon) + \frac{A_1}{A_2}\sigma_{22}(\sigma_L, d - x_1, x_2, x_3, a_2, b_2, \upsilon) \tag{8b}$$

$$\sigma_{33} = \sigma_{33}(\sigma_L, x_1, x_2, x_3, a_1, b_1, \upsilon) + \frac{A_1}{A_2}\sigma_{33}(\sigma_L, d - x_1, x_2, x_3, a_2, b_2, \upsilon) \tag{8c}$$

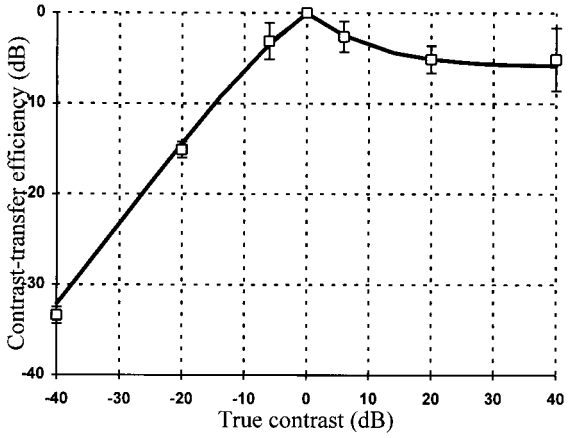

Figure 3. Contrast-transfer efficiency curve. The zero dB ordinate is the ideal contrast-transfer efficiency. ——: Theoretically predicted observed contrast-transfer efficiency [from Eq. (10)]. — □ —: contrast transfer-efficiency measured from simulated elastograms [28]. Observe the close match between theory and simulation.

where d is the total depth of the target and A is the area of the compressor whose subscript denotes the respective compressor.

The stress components at the face of compressor 2 are related to the corresponding components at the face of compressor 1 by the ratio of the area of compressor 1 to the area of compressor 2. In a target with infinite sides, the superposition involving the top and the bottom boundaries can be derived from Equation (8) [26,27]. Elastography in relatively homogeneous targets (discussed below) could then be described by Equation (5a), where the local longitudinal strains e_{11} are measured ultrasonically, the values for the three components of normal stress are estimated using Equation set (8), a value close to 0.5 is assumed for the Poisson's ratio, and the local computed values of the moduli E are displayed as an elastogram [5].

The simplifying assumptions built into the modified Love's theory gives rise to two types of errors. The first is due to the finite dimension of the elastic target along the transverse direction which is assumed to be infinite, and the second is due to the presence of elastic inhomogeneities in the target that is assumed to be relatively homogeneous, to within a modulus contrast of ± 6 dB. The errors due to the finite size of the target were discussed by Konofagou et al. [30], who showed that for target sizes equal to or larger than four compressor dimensions, the semi-infinite assumption is excellent. The errors due to deviation from the homogeneity assumption may be treated in terms of a contrast-transfer efficiency (CTE) parameter [28]. Since the displayed parameter in elastography is the strain (or a ''Love [25] corrected'' strain) and not the elastic modulus directly, one must know how close to the true stiffness distribution the strain distribution comes. Stated another way, for a given contrast in elastic modulus, what is the corresponding strain contrast in the elastogram? The CTE is defined by Ponnekanti et al. [28] as the ratio of the observed strain contrast from the elastogram to the true modulus contrast. Expressed in decibels, it is given by

$$CTE(dB) = |C_o(dB)| - |C_t(dB)|, \tag{9}$$

where C_o is the observed contrast and $C_t = E_I/E_M$ is the true

target elasticity contrast; the ratio of target (E_t) to background (E_M) Young's modulus. In Equation (9) the magnitude is used to have efficiency normalized to the 0 dB level; i.e. the maximum efficiency is reached at 0 dB for both hard and soft inclusion. Figure 3 shows the behavior of the CTE parameter over an 80-dB dynamic range of ''true'' modulus contrast. It is clear from the figure that for low modulus contrast levels (a high level of target modulus homogeneity), the elastographic strain contrast is nearly equal to the modulus contrast (CTE $\approx$ 1, or 0 dB). Hard inclusions have a relatively high level of CTE. However, soft inclusions that are completely surrounded by harder background material have a low CTE, and thus may not be well visualized by elastography. The reason for this limitation lies in the fact that, because of the incompressible nature of soft tissues (Poisson's ratio $\sim$ 0.5), the soft inclusion will be so constrained that it will not be able to deform under pressure as it might without constraints, thus assuming instead elastic properties that are closer to those of the surrounding material. This property of elastography represents a fundamental limitation that has been verified by finite-element simulations [28]. This observation was also corroborated theoretically by Kallel et al. [29]. Their analytic expression predicting the observed contrast in elastograms, as also shown in the Figure 3, is given as

$$\frac{1}{C_o} = \left[\frac{(1 - 2\nu)}{C_t + (1 - 2\nu)} + \frac{2}{1 + C_t(3 - 4\nu)}\right], \qquad (10)$$

As Equation (10) also suggests, the observed contrast is independent of the size and location of the inclusion. This indeed was also found by Ponnekanti et al. [28] using computer simulation. Equation (10) shows that the observed contrast is a function of the Poisson's ratio. However, for small variations of the Poisson's ratio which is assumed constant in tissue, the corresponding variation in the predicted contrast is small. Thus, the predicted observed contrast depends almost entirely on the true contrast.

It is to be noted that Love's model makes the assumption that the compressor is uniformly loaded, while elastography is performed by uniformly displacing the target surface through a small distance which results in a nonuniform loading of the compressor [4]. This discrepancy in the boundary conditions causes errors in the regions that are close to the compressor surface, which diminish in deeper regions in the target [25]. The implications of applying a constant displacement versus a constant stress were discussed by Konofagou et al. [30], who also described a displacement apodization technique for eliciting near-constant stress conditions in the vicinity of the compressor.

For elastograms to represent the distribution of the absolute Young's moduli, it is necessary to measure the load applied by the compressor (σ_L). For a uniformly loaded compressor, as is the case in Love's model, it is simply a multiplicative factor in Equations (7) that scales the distribution of stress inside the target. This load may be estimated by interposing a layer of elastic material with known modulus between the compressor and the target [17].

The approach to elastography described above generally results in several elastographic image artifacts. Notable among these are the target-hardening artifact [17] and the stress concentration artifacts near inclusions. These artifacts are a direct result of the assumption of uniform stress that is described above. It is also responsible for the less than ideal CTE [28,29]. The material below addresses the improvements in these artifacts and in the CTE as a result of relaxing this assumption.

2. Quantitative Strain Imaging and Elasticity Reconstruction. As discussed above, elastography based on quantitative strain imaging suffers from artifacts and fundamental limitations on CTE. To go beyond such limitations, elastography must be considered within the framework of IP solutions.

The IP approach is used extensively in electromagnetics, optics, and geophysics research [47]. In the biomedical field it has been extensively studied in bioelectricity to determine the distribution of potentials at the surface of the heart or the brain from a limited number of peripheral potential measurements. It is also known in the field of continum mechanics and biomechanics [48–51].

Recently, a few groups independently considered elastography as being a new challenging IP [31–35,37–40]. Below, we summarize the approach proposed by Kallel and Bertrand to solve this IP [38].

A method for solving the IP in elastography. The approach that we recently proposed to solve the IP in elastography is based on the use of a linear perturbation method. It consists essentially of minimizing the least squares error between observed and predicted displacement field. The predicted displacement field is obtained using a theoretical model of the elasticity equations (constitutive equations). This model may be represented by a general mapping function $\mathcal{J}$ that maps a tissue elasticity distribution into a displacement field. Mathematically this may take the following form:

$$\mathcal{J}: \mathbb{R}^{p+} \rightarrow \mathbb{R}^3$$

$$E \mapsto \mathcal{J}(E) = U = (u_1, u_2, u_3), \qquad (11)$$

where $\mathbb{R}^{p+}$ represents the set of the real positive numbers where the tissue elasticity distribution is defined; p defines the number of parameters needed to fully characterize the tissue elasticity distribution; as will be seen below, this number depends on the model and the symbol $\mapsto$ means that the elasticity distribution (E) is mapped to a displacement field (U). The quantity $U = (u_1, u_2, u_3)$ is the 3D tissue displacement vector field. The mapping function itself $\mathcal{J}$ is defined by the constitutive equations (stress–strain relationships) and the boundary conditions.

Defining general constitutive equations is a complex matter for soft tissues as these are nonlinear, viscoelastic, and anisotropic materials. However, as discussed above under certain stress–strain conditions, soft tissues can be thought as being elastic materials for which the generalized Hooke's law is used as constitutive equations. In that case, 81 constants are needed to fully characterize the tissue elastic properties. As is often done, these are reduced to nine, five, or two constants for orthotropic, transversely isotropic, and isotropic materials respectively [4]. When the tissue behaves as a nonlinear material the constitutive equation should be determined experimentally using a given strain–energy density function [4].

We have made numerous simplifications of the forward problem. Indeed, the tissue is assumed to behave as an inhomogeneous isotropic linear elastic medium [31–35]. Moreover, the ideal tissue is assumed to be incompressible. Hence, only one parameter is needed to define the tissue elastic properties. This parameter is known as the shear modulus (μ) or the Young's modulus (E). For an incompressible material for which the Poisson's ratio ν

is equal to 0.5, the Young's modulus is equal to 3μ. In our work, to simplify the numeric implementation of the model we assumed a Poisson's ratio close to 0.5 (0.495), thus relaxing the tissue incompressibility condition. In addition, since only the components of the displacement field in the acoustical scanning plane can be measured, we assume a plane–strain state problem for which out of plane motions are neglected [31–34].

After stating and fully defining a forward problem (FP) in elastography, we now can solve the corresponding IP. Solving this IP may be considered as an optimization problem for which the solution is defined as that which best reproduces an observed set of internal displacements. For such optimization problem, we need to define an objective function to be minimized [41]. The least squares error (or the generalized least squares error) is often used as an objective function since it provides an explicit analytic formulation of the solution. For our specific problem the solution is given by:

$$\hat{E} = \arg\min_{E \in \Re^+} \|\mathcal{J}(E) - U\|^2, \tag{12}$$

where $\hat{E}$ is the reconstructed elasticity distribution (Young's modulus distribution), $\mathcal{J}(E)$ is the predicted displacement field, and U is the observed displacement field. Since $\mathcal{J}(E)$ is a nonlinear function of E, we solve Equation (12) iteratively under the framework of the Newton–Raphson algorithm. Following this, we can show that at a given iteration k the elasticity distribution should be updated to

$$\begin{aligned} E_{k+1} &= E_k + \Delta E_k \\ \Delta E_k &= [S_k^T S_k]^{-1} S_k^T \Delta U_k \end{aligned} \tag{13}$$

where $S_k = \mathcal{J}'(E_k)$ is the Jacobian matrix that we also label the sensitivity matrix (to be discussed further below), T stands for matrix transpose, ΔE_k is the updating elasticity vector (elastic perturbation) and $\Delta U_k = U - U_k$ is the difference between observed (U) and predicted (U_k) displacement field, i.e., the displacement perturbation. At the first iteration the tissue is assumed to be homogeneous with known Young's modulus. At each iteration the elasticity distribution is updated according to Equation (13) and used to compute a new sensitivity matrix. The iteration process may be stopped when the updating elasticity is less than a prescribed value.

In practice, we found the matrix to be inverted in Equation (13) to be highly ill-conditioned, which makes the solution unstable. For conditioning, a Tikhonov regularization scheme is used. Underlying this regularization is the introduction of a compromise between fidelity to the noisy data and to *a priori* information about the solution [42]. Following this, the regularized updating term of Equation (13) is now given by [38,39]

$$\Delta E_k = [S_k^T W_k S_k + \lambda_k Q_k]^{-1} S_k^T W_k \Delta U_k \tag{14}$$

where W_k, Q_k are positive definite square matrices used to add constraint on the data and a priori information about the solution respectively, and λ_k is the regularization parameter used to quantify the compromise between fidelity to the data and the *a priori* information. In this article, the generalized cross-validation technique is used to find, in a least mean squares sense, the optimal regularization parameter [38,43], and the identity matrices are used for both W_k and Q_k. For large value of the regularization parameter λ_k, using the identity matrix for Q_k is equivalent to constraining the elastic perturbation ΔE_k to have only small values.

The sensitivity matrix. The sensitivity matrix S_k in Equation (13) is computed columnwise using the FP. Each column of this matrix is analogous to a system impulse response (i.e., sample of a Green's function). In this system the input is a local small elastic inhomogeneity (elastic perturbation) and the output is the displacement field perturbation vector. It is computed as follows. For a plane–strain state problem the finite element (FE) formulation of the FP is reduced to the solution of a $2n \times 2n$ system of equations defined as [44]:

$$[K]\{U\} = \{F\}, \tag{15}$$

where $[K]$ is a $2n \times 2n$ matrix known as the stiffness matrix which depends of the Young's modulus distribution, $\{U\}$ is a $2n \times 1$ vector defining the nodal displacements (both axial and lateral), and $\{F\}$ is a $2n \times 1$ vector defining the applied external forces and the body forces (in our model the body forces are neglected) [4]. After taking the partial derivative of the left- and righthand sides of Equation (15) with respect to the Young's modulus E we have

$$\left[\frac{\partial K}{\partial E_j}\right]\{U\} + [K]\left\{\frac{\partial U}{\partial E_j}\right\} = \left\{\frac{\partial F}{\partial E_j}\right\} \tag{16}$$

where E_j is the Young's modulus at element number j [a given spatial position in the region of interest (ROI)]. Assuming a known force distribution under the lower surface of the compressor means that forces should be used as boundary conditions; in that case the righthand side of Equation (16) vanishes. Hence, after some matrix manipulations we find that the jth column from the sensitivity matrix is given by

$$\left\{\frac{\partial U}{\partial E_j}\right\} = -[K]^{-1}\left[\frac{\partial K}{\partial E_j}\right][K]^{-1}\{F\} = S^{(j)} \tag{17}$$

Equation (17) defines the sensitivity matrix for a force-driven elastography problem, which in practice would require force sensors under the compressor. A different formulation must be developed for the more common displacement-driven elastography problem [40].

Simulation results. To emphasize the importance of modulus reconstruction versus simple quantitative strain imaging, we consider the elasticity distribution shown in Figure 4a. This modulus distribution is a cross section from a block of tissue embedding two circular inclusions. The Young's modulus of the background is set to 21 kPa and the inclusions are three times harder. Figure 4b shows the strain image obtained after applying 210 Pa uniform pressure on the top of the tissue block while assuming a perfect non-slip boundary conditions at the upper and lower surface of the tissue. As shown, this strain image (elastogram) could suggest the presence of a small soft inclusion in the middle of the ROI. This artifactual inclusion results from the high stress concentration occurring between the two hard inclusions which act as internal boundary conditions. This misinterpretation is a typical artifact occurring if the strain image is considered as a relative

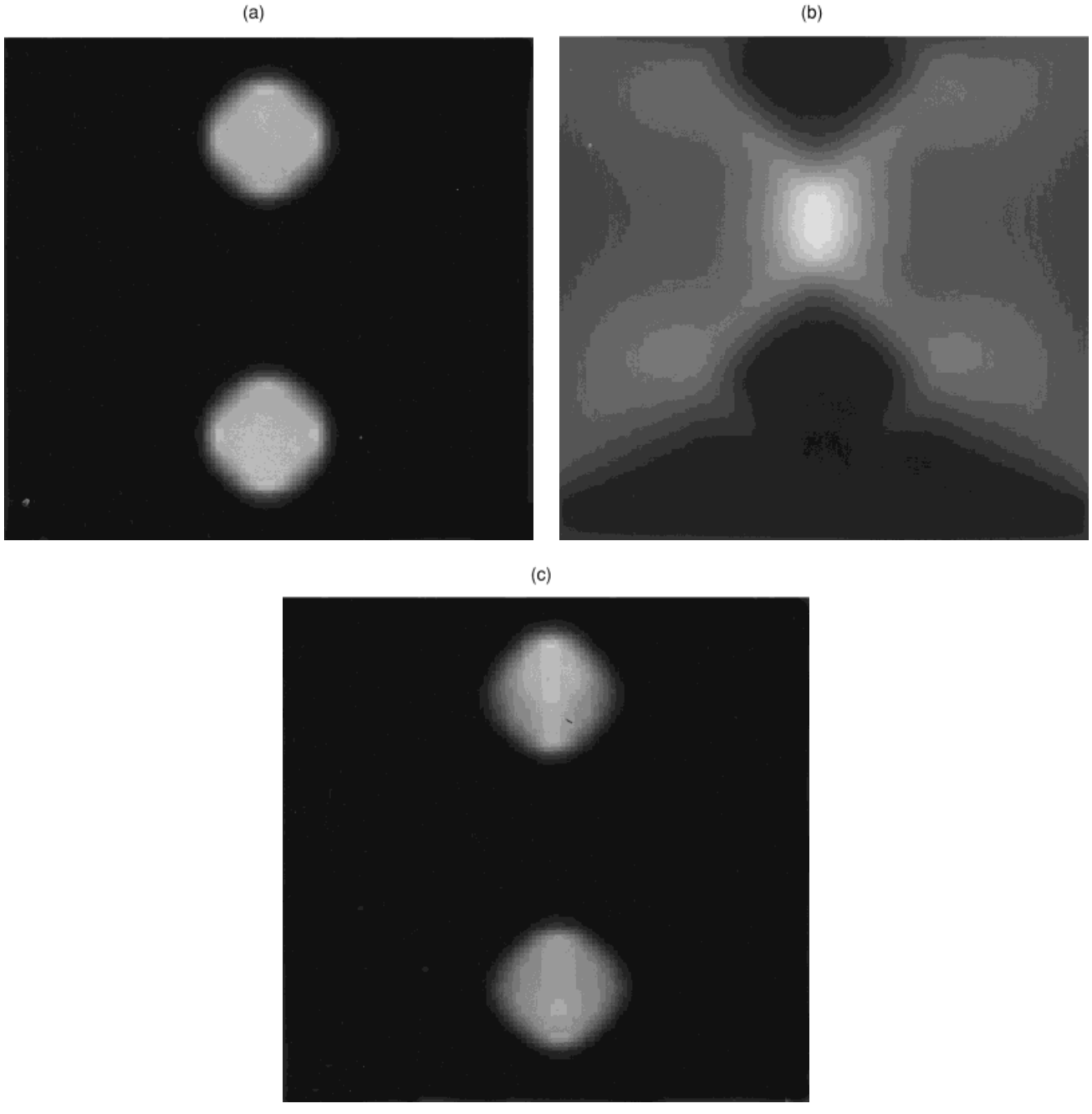

Figure 4. Simulated elasticity distribution and a corresponding strain image (elastogram). (a) Cross section in the acoustical scanning plane from the simulated modulus distribution. The size of the region of interest is 100 × 100 mm. The homogeneous medium is embedding two bounded circular inclusions that are three times harder than the background. (b) Strain image of the modulus distribution shown in (a) resulting from the application of a uniform pressure on the top and assuming a no-slip boundary condition on both the top and the bottom. Observe a white spot in the middle of the region of interest, suggesting the presence of a soft inclusion. (c) Reconstructed modulus distribution of (a) obtained after a total number of 15 iterations of the linear perturbation method applied on the noise-free axial displacement field (ideal). In this case CTE ≈ -2 dB.

measure of the tissue elasticity distribution. However, as shown in Figure 4c, when we solve the IP using the approach described above, the reconstructed modulus distribution is free of artifacts. Indeed, this reconstructed modulus distribution compares favorably to the original elastic modulus distribution shown in Figure 4a. Hence, solving the IP in elastography reduces strain imaging artifacts considerably.

As stated before and as shown by Figure 3, quantitative strain imaging suffers from a fundamental limitation on CTE. Using computer simulations, we have recently shown by simulation that solving the IP in elastography dramatically improves the CTE [37,39]. These simulations consisted of the reconstruction of a circular inclusion for which the modulus contrast was varied from -16 to 16 dB. The simulation results, summarized in Figure 5,

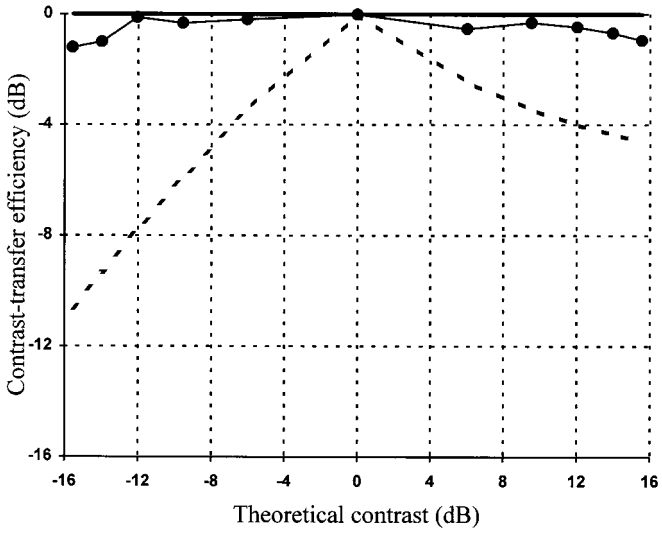

Figure 5. Contrast-transfer efficiency curves (CTE). (——): Ideal CTE; (— ● —) CTE measured from the reconstructed elasticity distribution which is obtained using the noise free axial displacement field. (----): theoretical CTE as predicted using Equation (10). Observe that after solving the IP in elastography the CTE is considerably increased and becomes close to the ideal CTE (0 dB).

clearly demonstrate the potential of solving the IP in increasing the CTE and therefore in overcoming the fundamental limitation of quantitative strain imaging [28].

C. Strain-to-Elastogram Transformation. The transformation of the actual strain distribution in the tissue into an elastogram involves the use of pulsed-echo ultrasound to estimate the longitudinal components of the local strain. The involvement of ultrasonic techniques means that some corruption of the actual strain data is inevitable, since the ultrasonic estimation of strain is inherently a noisy process. As shown in Equation (1) above, the estimation of the strain involves time delay estimation (TDE). These methods are well developed in the literature [53–57], but need to be modified further in the case of elastography owing to the unavoidable distortion in the postcompression signal due to the compression of the unresolvable acoustic scatterers contained in the tissue. This distortion means that the normalized cross-correlation coefficient function that is used to estimate time delay between the precompression and postcompression signals never achieves a unity peak value, as it would if only pure time delay were involved [52]. Thus, for large local tissue strains (typically >1–2%), this distortion bounds the performance of the elastogram. For very small local tissue strains, on the other hand, the performance of the elastogram is dominated by the classical lower bound on the attainable variance of TDE, the CRLB. It is therefore expected that the performance of elastography will somehow be optimal between these two bounds.

This concept has recently been elucidated with the aid of a general theoretical framework known as the strain filter (SF) by Varghese and Ophir [58]. The SF describes the relationship among the resolution, dynamic range, sensitivity, and elastographic *SNR* (also known as *SNRe*), and may be plotted as a graph of the upper bound of the *SNRe* versus the strain experienced by the tissue, for a given level of desired elastographic axial resolution as determined by the data window length. The ideal SF has an infinitely high, flat all-pass characteristic shape in the strain domain, which means that all local tissue strains are displayed in the elastogram with infinite *SNRe*; it also means that the strain dynamic range in the elastogram is infinite as well. Practical SFs have a bandpass characteristic shape in the strain domain, where the -3 dB width of this bandpass characteristic may be defined as the elastographic dynamic range. The low-strain behavior of the SF is determined by the variance as computed from the CRLB; the high-strain behavior of the SF is determined by the rate of decorrelation of a pair of congruent signals due to tissue distortion. A typical appearance of a group of SFs is shown in Figure 6, where the effect of changing the center frequency is used as a parameter. Observe that both the *SNRe* and the dynamic range of the elastogram corresponding to this SF increase with increasing center frequency. The exact shape of the SF is determined by the bandwidth, center frequency, sonographic *SNR*, and processing algorithm used in the elastography process. The improvement in the elastogram quality (see Fig. 2) obtained by varying the center frequency is illustrated in Figure 7. Note that with an increase in the center frequency from 3.5 to 7.5 MHz the elastograms become less noisy (observe the elastogram sequence from Fig. 7a–c) showing the increase in SNRe. The detail in the elastogram also improves due to the increase in the sensitivity and elastographic dynamic range. The resolution is maintained constant in all the elastograms shown in Figure 7.

The SF makes it possible to select the appropriate ultrasound system and signal-processing parameters to obtain the best possible elastogram. Tradeoffs among different parameters and techniques that enhance elastogram quality may also be evaluated and quantitatively predicted using the SF [59–64]. Signal-processing algorithms improve the correlation coefficient between the pre- and the postcompression signals, which is also incorporated into the SF.

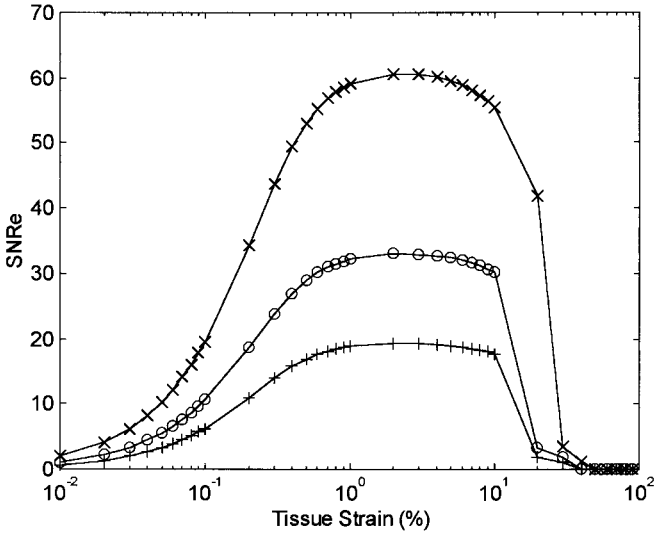

Figure 6. A group of strain filters for center frequencies of 3.5 MHz (+++), 5 MHz (⊖ ⊖ ⊖), and 7.5 MHz (x x x), respectively, with a 50% bandwidth and $T = 3$ mm (3.9 μs). Note the improvement in SNR_e, sensitivity, and dynamic range obtained with an increase in the pulse center frequency for a given resolution. The maximum attainable SNR_e is approximately proportional to the square of the center frequency.

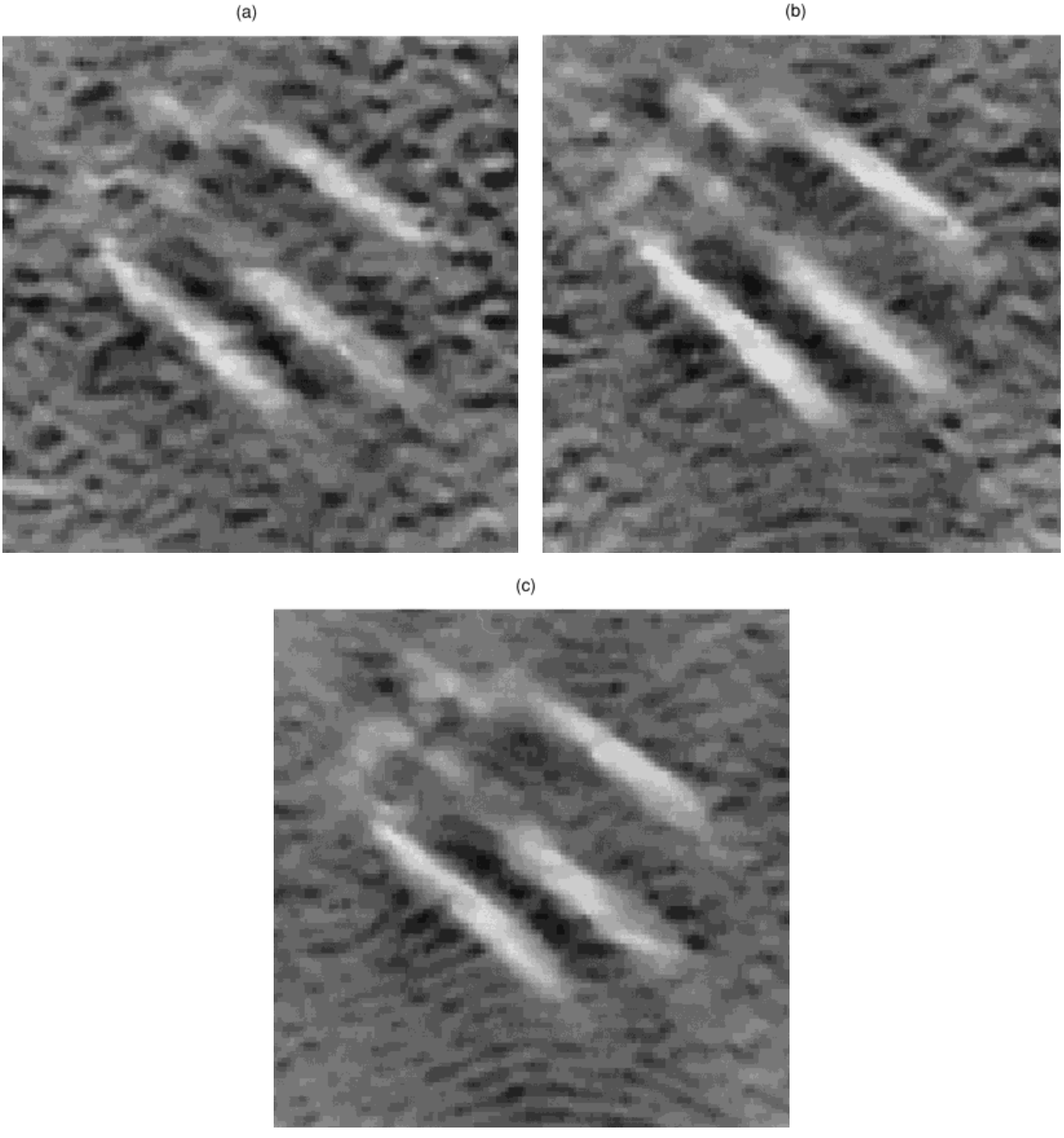

Figure 7. Elastograms obtained for center frequencies of (a) 3.5 MHz, (b) 5 MHz, and (c) 7.5 MHz, respectively, with a 50% bandwidth and $T = 3$ mm (3.9 μs). These elastograms correspond to the strain filters shown in Figure 6. Note the improvement in SNR_e (reduction in the noisy appearance in the elastogram), sensitivity and dynamic range (increase in elastogram detail) obtained with an increase in the pulse center frequency, as predicted by the strain filters. Note also that all these images were obtained via simulations where the beam characteristics have not changed; the improvements seen in the elastograms in going from (a) to (b) and (c) are strictly due to the effect of the strain filters shown in Figure 6. Panel (c) bears the strongest resemblance to Figure 2b, which is the ideal elastogram of this target.

A. Noise Sources. Development of the SF concept is based on obtaining the tightest bound on the variance of the strain estimator that includes all noise sources. Since the strain estimator uses TDE (displacement) to compute strain [Eq. (1)], the vast literature on TDE can be adapted for the strain estimation problem.

The CRLB is the most commonly used lower bound on time-delay variance [53–56]. While sonographic and quantization noise contributions are accounted for in the expression for the CRLB through the *SNR* term (sonographic *SNR* denoted by SNR_S) [53–56], the added effect of decorrelation on the variance of the

time delay estimate was modeled recently by Walker and Trahey [57]. The authors also indicated that TDE performance can be worse than the CRLB at poor SNR_S ($<$15 dB) and low correlation coefficient values ($<$0.5).

Signal decorrelation, a significant source of error in the displacement estimate, increases rapidly with tissue compression. Decorrelation errors are caused by the relative displacement of the scatterers in all three dimensions owing to tissue compression. Decorrelation errors increase with applied strain, causing a decay in the values of the correlation coefficient. The correlation coefficient with motion compensation due to axial deformation of elastic tissue for a 2D Gaussian model has been derived by Meunier and Bertrand [65] and is given by:

$$\rho = \frac{2\sqrt{\alpha\beta}}{\sqrt{2(\alpha^2 + 1)(\beta^2 + 1)}}\, e^{-1/2(f/\sigma_u)^2[(\alpha-1)^2/(\alpha^2+1)]} \tag{18}$$

where f is the spatial frequency in cycles per millimeter ($f = 2f_o/c$; c is the speed of sound in tissue = 1.54 mm/s); and σ_u is the standard deviation of the Gaussian envelope in cycles per millimeter ($\sigma_u = 2\sigma_f/c$, and $\sigma_f = 1/2\pi\sigma_t$; σ_t is the spatial standard deviation and σ_f is the standard deviation of the Gaussian envelope in the frequency domain); and α represents the axial compression where $\alpha = 1 - \varepsilon$, and ε is the applied strain. The corresponding lateral expansion is denoted by β (with the incompressibility constraint $\alpha\beta = 1$).

Expressions for the CRLB [53–57] have been derived for flat bandlimited signal and noise spectra. However, the correlation coefficient in [65] is derived for a Gaussian-shaped spectrum rather than a rectangular spectrum. A reasonable approximation was obtained by Céspedes et al. [66] using a rectangular spectrum centered at the Gaussian center frequency with the same mean square amplitude value as the Gaussian spectrum. The equivalent noise spectral bandwidth [67, p. 141] is defined by:

$$B = \frac{\int_0^\infty P(f)\, df}{P(f)|_{\max}} \tag{19}$$

where B is the bandwidth of a rectangular spectrum with the same total power and peak amplitude as the Gaussian pulse spectrum $P(f)$.

Signal decorrelation may be modeled as a noise process that reduces the composite SNR_C in the echo signal. SNR_C is a combination of the constant sonographic noise level (SNR_S) and a varying component due to signal decorrelation, and is given by [58]:

$$SNR_C = \frac{SNR_S SNR_\rho}{1 + SNR_S + SNR_\rho} \tag{20}$$

where $SNR_\rho = \rho/1 - \rho$ converts the correlation coefficient to an SNR measure. This relationship, independently derived by Friemel [68] and by Céspedes et al. [69], enables the use of SNR_C in CRLB expressions in the literature that involve signal decorrelation. This allows incorporation of signal processing algorithms into the SF (discussed below), as long as their effect on the signal correlation can be computed. From Equation (20) we observe that SNR_C will always be bounded by the smallest value of either SNR_S or SNR_ρ.

Increasing signal decorrelation errors with applied strain reduce SNR_C, causing the strain estimation variance to exceed the CRLB (as also noted by Walker and Trahey [57]), thereby necessitating the need for a more advanced lower bound to predict the variance of the strain estimator. The modified Ziv–Zakai lower bound proposed by Weinstein and Weiss [53,54] is used to obtain an accurate lower bound.

B. The Ziv–Zakai Lower Bound (ZZLB) on TDE. Weinstein and Weiss presented plots of the lower bound of the time delay variance versus the postintegration SNR [53,54] (defined as a product of the bandwidth, data window length, and the SNR_C), which divide the postintegration SNR domain into three distinct regions (low, moderate, and high). Since SNR_C is the only parameter in the expression for the postintegration SNR that varies with applied strain, its value determines the appropriate lower bound.

The CRLB as shown in Equation (2) is applicable only to high postintegration SNR situations (at low strains). In this region the TDE is subject only to local errors (ambiguity-free mode of operation). At moderate SNR values, the lower bound exceeds the CRLB, and obeys the Barankin bound. In this region ambiguities in the signal phase cannot be resolved; however, an estimate of the TDE may still be obtained using the correlation between signal envelopes. At low postintegration SNR values, the lower bound approaches a constant level. In this region, both envelope and phase ambiguities exist, and the time delay cannot be estimated correctly. The thresholds separating these three regions are determined by the value of the postintegration SNR [53,54]. The above combination of lower bounds on the variance of the time-delay estimator is referred to as the Ziv–Zakai lower bound (ZZLB) [53,54]. The ZZLB provides the tightest bound on the variance of the TDE.

C. The Strain Filter in Elastography. A measure of elastographic image quality was described [19,46] in terms of the mean-to-standard deviation ratio (SNR_e) of the elastogram:

$$SNR_e = \frac{m_s}{\sigma_s} \tag{21}$$

where m_s and σ_s are, respectively, the mean and standard deviation of the strain estimates in a region of uniform elasticity. The upper bound of the SNR_e is obtained when the total applied strain (ε_t) and the lower bound on the strain estimation standard deviation (σ_{ZZLB}) are substituted in Equation (21):

$$SNR_e^{UB} = \frac{\varepsilon_t}{\sigma_{ZZLB}}. \tag{22}$$

The modified ZZLB expression for the strain estimation variance [58] is given by:

$$\sigma^2_{ZZLB} \geq \begin{cases} \dfrac{(\varepsilon T)^2}{6T\Delta t}, & BTSNR_C < \gamma \\ \text{Threshold} & \gamma < BTSNR_C < \delta \\ \dfrac{2\sigma^2_{BB}}{T\Delta t}, & \delta < BTSNR_C < \vartheta \\ \text{Threshold} & \vartheta < BTSNR_C < \eta \\ \dfrac{2\sigma^2_{CRLB}}{T\Delta t}, & \eta < BTSNR_C \end{cases} \tag{23}$$

where T is the length of the temporal window, $\Delta t = t_{1a} - t_{1b}$ is the overlap between successive windows, σ^2_{CRLB} represents the CRLB, and σ^2_{BB} represents the Barankin bound. The quantity $BTSNR_C$ is referred to as the postintegration SNR. Equation (23) shows the three distinct operating regions for σ^2_{ZZLB}, depending on the value of $BTSNR_C$. The strain variance is computed from the TDE variance using the expression derived by Walker and Trahey [57], as long as the ZZLB coincides with the CRLB. The Barankin bound exceeds the CRLB by a factor of $12(f_0/B)^2$ [53,54]. A distinct threshold region is observed between the CRLB and the Barankin bound; however, the variance increases exponentially in this threshold region. Accurate estimation of the strain is possible only within the CRLB. The threshold points used in Equation (23) are defined as follows:

$$\eta = \frac{2}{T\Delta t}\frac{6}{\pi^2}\left(\frac{f_0}{B}\right)^2\left[\varphi^{-1}\left(\frac{B^2}{24f_0^2}\right)\right]^2$$

$$\vartheta = \frac{2}{T\Delta t}\frac{2.76}{\pi^2}\left(\frac{f_0}{B}\right)^2$$

$$\delta = \frac{1}{T\Delta t}\varsigma$$

$$\gamma \approx \frac{2}{T\Delta t}0.46 \qquad (24)$$

where f_0 is the center frequency, B is the rectangular bandwidth, $\varphi^{-1}(y)$ is the inverse of $\varphi(y) = 1/\sqrt{2\pi}\int_y^\infty e^{-\mu^2/2}\,d\mu$, and $(\varsigma/2)\varphi(\sqrt{\varsigma/2}) = (12\pi/B\varepsilon T)^2$, which has two solutions. The larger value of ς is used to compute the threshold. When $\eta < BTSNR_C$, the ZZLB coincides with the CRLB, which is the ambiguity free region. If $\delta < BTSNR_C < \vartheta$, the ZZLB coincides with the Barankin bound, where phase ambiguities increase the TDE variance. Finally, when $BTSNR_C < \gamma$, the lower bound is characterized by the constant variance level of $(\varepsilon T)^2/6T\Delta t$, which corresponds to the variance of a random variable uniformly distributed between $[-\varepsilon T/2, \varepsilon T/2]$.

The variation of SNR_e^{UB} [Eq. (22)] with applied axial strain is defined as the SF. Three distinct regions constitute the SF, which depends on the appropriate lower bound that contributes to σ^2_{ZZLB} [Eq. (23)]. Decorrelation errors increase with applied strain [70], causing σ^2_{ZZLB} to move from the CRLB to the Barankin bound or the constant variance level as shown in Equation (23). The three distinct regions in Equation (23) are observed in plots of the strain filter as shown by the curves in Figure 3. When the lower bound coincides with the Barankin bound, the performance of the strain filter drops sharply, with a further drop in performance observed when the variance coincides with the constant variance level.

The range of strains that can be reliably depicted in an elastogram determines the dynamic range of the strain filter, which is defined as:

$$DR = 20\log_{10}\left[\frac{\varepsilon_{\max}}{\varepsilon_{\min}}\right], \qquad (25)$$

where $\varepsilon_{\max}$ is the maximum strain and $\varepsilon_{\min}$ is the minimum strain at a specified SNR_e level in the strain filter. The quantity $\varepsilon_{\min}$ also defines the sensitivity of the strain filter.

III. DISCUSSIONS AND CONCLUSIONS

In this article we have described the elastographic process as a two-step system. The first component of the system involved the mapping of the actual distribution of the elastic moduli in the target (or tissue) into a distribution of local tissue strains. Under ideal conditions of target uniformity, semi-infinite target dimensions, and infinite compressor dimensions, this mapping is essentially perfect. In other words, the local stresses in the target are all uniform, and therefore the local strains are simply inversely proportional to the local elastic moduli; the corresponding value of the CTE is unity (0 dB).

Under realistic conditions such as target nonuniformity and finite target and compressor dimensions, the CTE that corresponds to this mapping shows values that are less than or equal to unity, and mechanical artifacts tend to appear in the elastogram. The mapping of the local moduli under these conditions becomes complicated. Kallel and Bertrand [38] demonstrated that the CTE can be significantly improved by iteratively solving the IP, and that the mechanical artifacts can be significantly reduced. This recursive IP block is also shown in Figure 1, where the input CTE is typically well below unity, while the output CTE is close to unity. The output of the recursive IP is therefore a closer approximation to the input modulus distribution. It should be noted that the choice of whether or not to engage the IP process is a matter of choice, which is dictated by a tradeoff between the desired image CTE, artifacts and the computational cost that might be incurred in achieving it.

The second component of the elastographic process is the formation of the elastogram via the use of ultrasonic pulsed-echo techniques. Since the strain along the ultrasonic beam axis is computed as the difference between two time delays, results from the literature on time delay estimation may be used. However, these results must be modified since in elastography the signal experiences slight distortions in addition to simple time shifts. These distortions come from the fact that the echo signals are speckle signals that result from the coherent summation of echoes from a multiplicity of unresolvable acoustic scatterers; the applied compression tends to slightly distort the geometrical relationships among these scatterers, resulting in distortions in the echo signals.

The Cramér–Rao lower bound on the variance of TDEs, described in the literature, is the limiting factor in the formation of the elastogram for very small local strains, where signal distortion is unimportant. This tends to be the case in regions that are relatively hard. On the other hand, regions that experience high values of strain tend to suffer from a significant amount of distortion. The region between these bounds may be described in terms of an SF that is typically a bandpass filter in the strain domain. This filter allows only a restricted range of strain values to be included in the elastogram. The deviation of the strain filter from an ideal all-pass characteristic in the strain domain is due to the ultrasound system parameters, the finite value of the sonographic SNR, and the effects of signal decorrelation. Signal decorrelation determines the largest value of strain that is accurately estimated, while SNR_S determines the smallest measurable strain value. The dynamic range of the system is thus limited on the low end by sonographic noise effects and on the high end by signal decorrelation, resulting in a bandpass filter in the strain domain.

This bandpass characteristic can be modified and improved

upon by proper selection of ultrasonic system parameters and by modifications to the methods and algorithms used for signal processing. It has been demonstrated, for example, that increasing the center frequency of the system results in a strain filter that is both taller and wider, indicating an improved level of SNR_e and a simultaneous enhancement of the sensitivity and broadening of the elastographic dynamic range. It has also been demonstrated that under certain conditions (i.e., optimal multicompression with signal stretching [64]), stretching the postcompression RF signal prior to TDE changes the bandpass characteristic of the strain filter into a more desirable highpass characteristic.

The shape of the strain filter defines the quality of the elastogram; a narrow, low filter will cause elastographic artifacts such as image noise and low dynamic range to plague the elastogram. Thus, the design of the optimal strain filter for a given situation is of utmost importance to the production of quality elastograms.

In conclusion, the combined IP approach to improve the CTE and reduction of artifacts, and the strain filter approach to improve the elastogram image quality hold promise for significant improvements in elastography in the future. It should be noted that the step involving the optimization of the strain filter must precede the IP step, since the elastogram serves as input to the IP procedure. The optimal combination of these should result in quality images of the modulus distribution itself.

REFERENCES

1. Y. C. Fung, *Biomechanical Properties of Living Tissues* (Springer Verlag, New York), 1981.
2. W. A. D. Anderson, *Pathology* (C. V. Mosby, St. Louis), 1953.
3. A. P. Sarvazyan, A. Skovoroda, and D. Vucelic. ''Utilization of surface acoustic waves and shear acoustic properties for imaging and tissue characterization,'' (1991) (abstr.).
4. S. Saada, *Elasticity, Theory and Applications* (Pergamon Press, New York), 1983.
5. T. A. Krouskop, D. R. Dougherty, and S. F. Levinson. ''A pulsed Doppler ultrasonic system for making noninvasive measurements of the mechanical properties of soft tissue,'' *J. Rehabil. Res. Dev.* **24,** 1–8 (1987).
6. K. J. Parker, S. R. Huang, R. A. Musulin, and R. M. Lerner. ''Tissue response to mechanical vibrations for sonoelasticity imaging,'' *Ultrasound Med. Biol.* **16,** 241–246 (1990).
7. S. F. Levinson. ''Ultrasound propagation in anisotropic soft tissues: the application of linear elastic theory,'' *J. Biomech.* **20,** 251–260 (1987).
8. A. P. Sarvazyan, ''Shear acoustic properties of soft biological tissues in medical diagnostics,'' in *J. Acoust. Society of America, Proceedings of the 125th Meeting,* Vol. 93, Part 2, 1993, p. 2329.
9. M. Walz, J. Teubner, and M. Georgi, ''Elasticity of benign and malignant breast lesions: Imaging, application and results in clinical and general practice,'' in *Eighth International Congress on the Ultrasonic Examination of the Breast,* 1993, p. 56.
10. I. M. Ariel and J. B. Cleary, *Breast Cancer Diagnosis and Treatment* (McGraw-Hill, New York), 1987.
11. B. D. Fornage, personal communication (1991).
12. M. Mridha and S. Ödman. ''Characterization of subcutaneous edema by mechanical impedance measurements,'' *J. Invest. Dermatol.* **5,** 575–578 (1985).
13. M. Mridha and S. Ödman. ''Noninvasive method for the assessment of subcutaneous edema,'' *Med. Biol. Eng. Comput.* **24,** 393–398 (1986).
14. G. S. Brody, T. J. Peng, and R. F. Landel, *The Rheological Properties of Human Skin and Scar Tissues: Bioengineering and the Skin.* R. Marks and P. A. Payne, Eds. (Int. Med. Public., Lancaster, United Kingdom), 1981.
15. X. T. Truong, S. R. Jarrett, and M. C. Nguyen. ''A method for deriving viscoelastic modulus for skeletal muscle from transient pulse propagation,'' *IEEE Trans. Biomed. Eng.* **BE-25,** 382–384 (1978).
16. J. Ophir, I. Céspedes, B. Garra, H. Ponnekanti, Y. Huang, and N. Maklad. ''Elastography: ultrasonic imaging of tissue strain and elastic modulus *in vivo,*'' *Eur. J. Ultrasound* **3,** 49–70 (1996).
17. J. Ophir, I. Céspedes, H. Ponnekanti, Y. Yazdi, and X. Li. ''Elastography: A method for imaging the elasticity in biological tissues,'' *Ultrasonic Imaging.* **13,** 111–134 (1991).
18. J. Ophir and Y. Yazdi, U.S. Patent 5,107,837 (1992).
19. I. Céspedes. ''Elastography: Imaging of biological tissue elasticity,'' Ph.D. dissertation, University of Houston, Department of Electrical Engineering, Houston, Texas, 1993.
20. I. Céspedes, J. Ophir, H. Ponnakanti, and N. Maklad. ''Elastography: elasticity imaging using ultrasound with application to muscle and breast *in vivo,*'' *Ultrasonic Imaging.* **15,** 73–88 (1993).
21. G. C. Foster, M. P. Embree, and W. D. O'Brien. ''Flow velocity profile via time-domain correlation: error analysis and computer simulation,'' *IEEE Trans. Ultrason. Ferroelect. Freq. Control.* **UFFC-37,** 164–174 (1990).
22. A. D. Whalen, *Detection of Signals in Noise* (Academic Press, New York), 1971.
23. E. I. Céspedes, M. F. Insana, and J. Ophir. ''Theoretical bounds on strain estimation in elastography,'' *IEEE Trans. Ultrason. Ferroelect. Freq. Control* **42,** 969–972 (1995).
24. J. Boussinesq, *Application des Potentiels a l'Etude de l'Equilibre et du Mouvement des Solides Elastiques* (Gauthier-Villars, Paris), 1885.
25. A. E. H. Love. ''The stress produced in a semi-infinite solid by pressure on part of the boundary,'' *Trans. Royal Soc. (Lond., Series A)* **228,** 337 (1929).
26. H. Ponnekanti, J. Ophir, and I. Céspedes. ''Axial stress distributions between coaxial compressors in elastography: an analytical model,'' *Ultrasound Med. Biol.* **18,** 667–673 (1992).
27. H. Ponnekanti, J. Ophir, and I. Céspedes. ''Ultrasonic imaging of the stress distribution in elastic media due to an external compressor,'' *Ultrasound Med. Biol.* **20,** 27–33 (1994).
28. H. Ponnekanti, J. Ophir, Y. Huang, and I. Céspedes. ''Fundamental mechanical limitations on the visualization of elasticity contrast in elastography,'' *Ultrasound Med. Biol.* **21,** 533–543 (1995).
29. F. Kallel, M. Bertrand, and J. Ophir. ''Fundamental limitations on the contrast-transfer efficiency in elastography: An analytic study,'' *Ultrasound Med. Biol.* **22,** 463–470 (1996).
30. E. Konofagou, P. Dutta, J. Ophir, and I. Céspedes. ''Reduction of stress nonuniformities by apodization of compressor displacement in elastography,'' *Ultrasonic Imaging* **17,** 50 (1995) (abstr.).
31. S. Y. Emelianov, A. R. Skovoroda, M. A. Lubinski, and M. O'Donnell, ''Reconstructive elasticity imaging,'' in *Acoustical Imaging 21.* J. P. Jones, Ed., Plenum Press, New York, 1995, pp. 241–252.
32. F. Kallel, M. Bertrand, J. Ophir, and I. Céspedes, ''Determination of elasticity distribution in tissue from spatio-temporal changes in ultrasound signals,'' in *Acoustical Imaging 21.* J. P. Jones, Ed., Plenum Press, New York, 1995, pp. 433–443.
33. K. R. Raghavan and A. E. Yagle. ''Forward and inverse problems in imaging the elasticity of soft tissue,'' *IEEE Trans. Nuclear Sci.* **41,** 1639–1647 (1994).
34. A. R. Skovoroda, S. Y. Emelianov, M. A. Lubinski, A. P. Sarvazyan, and M. O'Donnell. ''Theoretical analysis and verification of ultrasound displacement and strain imaging,'' *IEEE Trans. Ultrason. Ferroelect. Freq. Control* **41,** 302–313 (1994).
35. C. Sumi, A. Suzuki, and K. Nakayama. ''Estimation of shear modulus distribution in soft tissue from strain distribution,'' *IEEE Trans. Biomed. Eng.* **42,** 193–202 (1995).
36. J. G. Webster, *Electrical Impedance Tomography* (Adam Hilger, New York), 1990.
37. F. Kallel, M. Bertrand, J. Ophir, and I. Céspedes. ''Tissue elasticity reconstruction using a linear perturbation method: Performance analysis,'' *Ultrasonic Imaging* **17,** 51 (1995) (abstr.).

38. F. Kallel and M. Bertrand. ''Tissue elasticity reconstruction using linear perturbation method,'' *IEEE Trans. Med. Imag.* **15,** 299–313 (1996).
39. F. Kallel. ''Proprietes elastiques des tissus mous a partir de l'analyse des changements spatio-temporels dans les signaux ultrasonores,'' Ph.D. dissertation, Ecole Polytechnique, University of Montreal, Quebec, Canada, 1995.
40. F. Kallel, M. Bertrand, J. Ophir, and I. Céspedes. ''Advances in tissue elasticity reconstruction using linear perturbation method,'' in *Acoustical Imaging 22.* J. P. Jones, Ed., Plenum Press, New York, 1996, pp. 267–277.
41. E. G. Philip, W. Murray, and M. H. Wright, *Practical Optimization* (Academic Press, London), 1981.
42. G. Demoment. ''Image reconstruction and restoration: Overview of common estimation structures and problems,'' *IEEE Trans. Acoust. Speech Signal Proc.* **37,** 2024 (1989).
43. S. Galatsanos and A. Katsaggelos. ''Methods for choosing the regularization parameter and estimating the noise variance in image restoration and their relation,'' *IEEE Trans. Imag. Proc.* **1,** 322 (1992).
44. J. N. Reddy, *An Introduction to the Finite Element Methods* (McGraw-Hill, New York), 1984.
45. J. Meunier and M. Bertrand. ''Echographic image mean gray level change with tissue dynamics: A system-based model study,'' *IEEE Trans. Biomed. Eng.* **42,** 403 (1995).
46. E. I. Céspedes and J. Ophir. ''Reduction of image noise in elastography,'' *Ultrasonic Imaging* **15,** 89–102 (1993).
47. R. D. N. Ghosh, *Methods of Inverse Problems in Physics* (CRC Press, Boca Raton, FL), 1986.
48. H. D. Bui, *Introduction aux Problèmes Inverses en Mécanique des Matériaux* (Éditions Eyrolles, Paris), 1993.
49. Z. Gao and T. Mura. ''Non-elastic strains in solids: an inverse characterization from measured boundary data,'' *Int. J. Eng. Sci.* **30,** 55–68 (1992).
50. A. Zabras, N. Maniatty, and K. Stelson. ''Finite element analysis of some inverse elasticity problems,'' *J. Eng. Mech.* **115,** 1303–1317 (1989).
51. J. P. Laible, D. Pflaster, B. R. Simon, N. H. Krag, M. Pope, and L. D. Haugh. ''A dynamic material parameter estimation procedure for tissue using a poroelastic finite element model,'' *J. Biomed. Eng.* **116,** 19–29 (1994).
52. F. Kallel and M. Bertrand, ''A note on strain estimation using correlation techniques,'' *1993 IEEE Ultras. Symp. Proc.,* 883–887 (1993).
53. E. Weinstein and A. Weiss. ''Fundamental limitations in passive time delay estimation—part I: Narrow-band systems,'' *IEEE Trans. Acoust. Speech Signal Proc.* **ASSP-31,** 472–485 (1983).
54. E. Weinstein and A. Weiss. ''Fundamental limitations in passive time delay estimation—part II: Wide-band systems,'' *IEEE Trans. Acoust. Speech Signal Proc.* **ASSP-31,** 1064–1078 (1984).
55. A. H. Quazi. ''An overview of the time delay estimate in active and passive systems for target localization,'' *IEEE Trans. Acoust. Speech Signal Proc.* **ASSP-29,** 527–533 (1981).
56. C. H. Knapp and G. C. Carter. ''The generalized correlation method for estimation of time delay,'' *IEEE Trans. Acoust. Speech Signal Proc.* **ASSP-24,** 320–327 (1976).
57. F. W. Walker and E. G. Trahey. ''A fundamental limit on delay estimation using partially correlated speckle signals,'' *IEEE Trans. Ultrason. Ferroelect. Freq. Control* **42,** 301–308 (1995).
58. T. Varghese and J. Ophir. ''A theoretical framework for performance characterization of elastography: The strain filter,'' *IEEE Trans. Ultrason. Ferroelect. Freq. Control* (in press).
59. M. Bilgen and M. F. Insana. ''Deformation models and correlation analysis in elastography,'' *J. Acoust. Soc. Am.* **99,** 3212–3224 (1996).
60. Y. Huang, E. I. Céspedes, and J. Ophir. ''Techniques for noise reduction in elastograms,'' *American Institute of Ultrasound and Medicine* (1995) (abstr.).
61. T. Varghese, J. Ophir, and E. I. Céspedes. ''Noise reduction in elastography using temporal stretching with multicompression averaging,'' *Ultrasound Med. Biol.* **22,** 1043–1052 (1996).
62. S. K. Alam and J. Ophir. ''Reduction of signal decorrelation from mechanical compression of tissues by temporal stretching,'' *Ultrasound Med. Biol.* (in press).
63. T. Varghese and J. Ophir. ''Enhancement of echo-signal correlation in elastography using temporal stretching,'' *IEEE Trans. Ultrason. Ferroelect. Freq. Control* (in press).
64. T. Varghese and J. Ophir. ''Performance optimization in elastography: Multicompression with temporal stretching,'' *Ultrasonic Imaging* (in press).
65. J. Meunier and M. Bertrand. ''Ultrasonic texture motion analysis: Theory and simulation,'' *IEEE Trans. Ultrason. Ferroelect. Freq. Control* **14,** 293–300 (1995).
66. E. I. Céspedes, Y. Huang, J. Ophir, and S. Spratt. ''Methods for estimation of subsample time delays of digitized echo signals,'' *Ultrasonic Imaging* **17,** 142–171 (1995).
67. J. S. Bendat and A. C. Piersol, *Random Data: Analysis and Measurement,* 2nd ed. (Wiley, New York), 1986.
68. B. H. Friemel, ''Real-time ultrasonic two-dimensional vector velocity estimation utilizing speckle-tracking algorithms: Implementation and limitations,'' Ph.D dissertation, Duke University, 1994.
69. E. I. Céspedes, J. Ophir, and S. K. Alam. ''The combined effect of signal decorrelation and random noise on the variance of time-delay estimation,'' *IEEE Trans. Ultrason. Ferroelect. Freq. Control* (in press).
70. M. O'Donnell, A. R. Skovoroda, and B. M. Shapo. ''Measurement of arterial wall motion using Fourier based speckle tracking algorithms,'' *Proc. 1991 IEEE Ultras. Symp.,* 1101–1104 (1991).